Potential of Magnetic Hyperthermia to Stimulate Localized Immune Activation

Thomas J. Carter, Giulia Agliardi, Fang-Yu Lin, Matthew Ellis, Clare Jones, Mathew Robson, Angela Richard-Londt, Paul Southern, Mark Lythgoe, May Zaw Thin, Vyacheslav Ryzhov, Rafael T. M. de Rosales, Cordula Gruettner, Maha R. A. Abdollah, R. Barbara Pedley, Quentin A. Pankhurst, Tammy L. Kalber, Sebastian Brandner, Sergio Quezada, Paul Mulholland, Maxim Shevtsov, and Kerry Chester*

Magnetic hyperthermia (MH) harnesses the heat-releasing properties of superparamagnetic iron oxide nanoparticles (SPIONs) and has potential to stimulate immune activation in the tumor microenvironment whilst sparing surrounding normal tissues. To assess feasibility of localized MH in vivo, SPIONs are injected intratumorally and their fate tracked by Zirconium-89-positron emission tomography, histological analysis, and electron microscopy. Experiments show that an average of 49% (21–87%, $n = 9$) of SPIONs are retained within the tumor or immediately surrounding tissue. In situ heating is subsequently generated by exposure to an externally applied alternating magnetic field and monitored by thermal imaging. Tissue response to hyperthermia, measured by immunohistochemical image analysis, reveals specific and localized heat-shock protein expression following treatment. Tumor growth inhibition is also observed. To evaluate the potential effects of MH on the immune landscape, flow cytometry is used to characterize immune cells from excised tumors and draining lymph nodes. Results show an influx of activated cytotoxic T cells, alongside an increase in proliferating regulatory T cells, following treatment. Complementary changes are found in draining lymph nodes. In conclusion, results indicate that biologically reactive MH is achievable in vivo and can generate localized changes consistent with an anti-tumor immune response.

1. Introduction

Hyperthermia has been applied clinically for cancer treatment, either as a monotherapy or in combination with other treatment modalities such as ionizing radiation and chemotherapy.[1–5] The approach has met with some success in difficult to treat tumors. For example, in a phase III randomized clinical trial (EORTC 62961-ESHO 95), a combination of regional hyperthermia and neoadjuvant chemotherapy resulted in increased local progression-free survival as well as improved overall survival for patients with localized high-risk soft tissue sarcoma.[6]

Clinical hyperthermia treatment involves the increase of local temperature (within the range of 43–46 °C) resulting in tumor cell apoptosis/necrosis, reportedly due in part to the relatively high susceptibility of malignant cells to hyperthermia, as compared to normal cells.[7] The hypoxic tumor microenvironment and the increased mitotic rate of malignant cells have also been shown to predispose cancer cells to

Dr. T. J. Carter, Dr. G. Agliardi, M. Robson, Dr. M. Abdollah,
Prof. R. B. Pedley, Prof. S. Quezada, Dr. P. Mulholland, Prof. K. Chester
UCL Cancer Institute
University College London (UCL)
Paul O'Gorman Building, 72 Huntley Street, London WC1E 6DD, UK
E-mail: k.chester@ucl.ac.uk
Dr. F. Lin, Dr. P. Southern, Prof. Q. Pankhurst
UCL Healthcare Biomagnetics Laboratory
21 Albermarle Street, London W1S 4BS, UK

The ORCID identification number(s) for the author(s) of this article can be found under https://doi.org/10.1002/smll.202005241.

Dr. M. Ellis, A. Richard-Londt, Prof. S. Brandner
Division of Neuropathology
Department of Neurodegenerative Disease
UCL Queen Square Institute of Neurology
Queen Square, London WC1N 3BG, UK
Dr. M. Ellis
Cancer Sciences Unit
Cancer Research UK Centre
University of Southampton
Somers Building, Southampton SO16 6YD, UK
Dr. C. Jones, Dr. R. T. M. de Rosales
School of Biomedical Engineering and Imaging Sciences
King's College London (KCL)
St Thomas' Hospital
London SE1 7EH, UK
Dr. P. Southern, Prof. Q. Pankhurst
Resonant Circuits Limited (RCL)
London W1S 4BS, UK

**ADVANCED
SCIENCE NEWS**
www.advancedsciencenews.com

**NANO · MICRO
small**
www.small-journal.com

temperature sensitivity.[8] Hyperthermia therapy can be divided into three main target temperature ranges: ablation therapy (>50 °C) which causes tissue death due to coagulation necrosis;[9] high temperature focal hyperthermia (>43 °C) leading to irreversible cell damage, delayed cell damage, ischemia and inflammatory infiltrates;[10,11] and moderate hyperthermia (38–43 °C) that aims to generate sub-lethal cell damage, increasing immune cell trafficking into tumors, thus increasing tumor immunogenicity.[12–15] Moderate hyperthermia is the best tolerated and most clinically translatable hyperthermia therapy but, as with all cancer hyperthermia treatments, a major challenge in treatment delivery is to confine the heating effect to tumor tissue, leaving healthy surrounding tissue undamaged. Nanotechnology offers an elegant solution to this problem, using heat-generating nanoparticles targeted to, or implanted within, tumors.

A range of different nanoparticles have been studied for their use in cancer hyperthermia including gold nanoparticles (AuNPs), carbon nanotubes, and superparamagnetic iron oxide nanoparticles (SPIONs).[16–21] SPIONs, the most clinically developed particle type, typically consist of a magnetic iron oxide core stabilized by biocompatible hydrophilic surface coatings such as polyethylene glycol, aminosilane, or dextran.[22] The magnetic properties and favorable biocompatibility of dextran-coated SPIONs make them the most attractive for clinical use and they have been approved for a range of applications; notably in magnetic resonance imaging (MRI), including hepatic MRI,[23] imaging macrophage density in atherosclerosis, and treatment of iron deficiency anemia.[23–28]

SPIONs release energy in the form of heat via hysteresis loss when exposed to an alternating magnetic field (AMF),[29] a process known as magnetic hyperthermia (MH). SPION-generated MH has strong potential for use in cancer treatment but administration remains a challenge because intravenously injected SPIONs are rapidly sequestered by the reticuloendothelial system (RES) within the liver and spleen, limiting their delivery to tumor tissue.[23] A number of approaches have been employed to increase tumor delivery, including targeting SPIONs to tumor cells, intra-arterial delivery, modifying SPION surface coatings, and blocking uptake of SPIONs by the RES.[16,22,30–32]

Despite these efforts, on average less than one percent of the injected SPION dose will reach the tumor;[33,34] insufficient quantities to conduct effective MH.

Prof. M. Lythgoe, Dr. M. Zaw-Thin, Dr. T. L. Kalber
Centre for Advanced Biomedical Imaging
Division of Medicine
University College London
London WC1E 6DD, UK
Dr. V. Ryzhov, Dr. M. Shevtsov
NRC "Kurchatov Institute"
Petersburg Nuclear Physics Institute
Gatchina 188300, Russia
Dr. C. Gruettner
Micromod Partikeltechnologie GmbH
Friedrich-Barnewitz-Str. 4, Rostock D-18119, Germany
Dr. M. Abdollah
Department of Pharmacology and Biochemistry
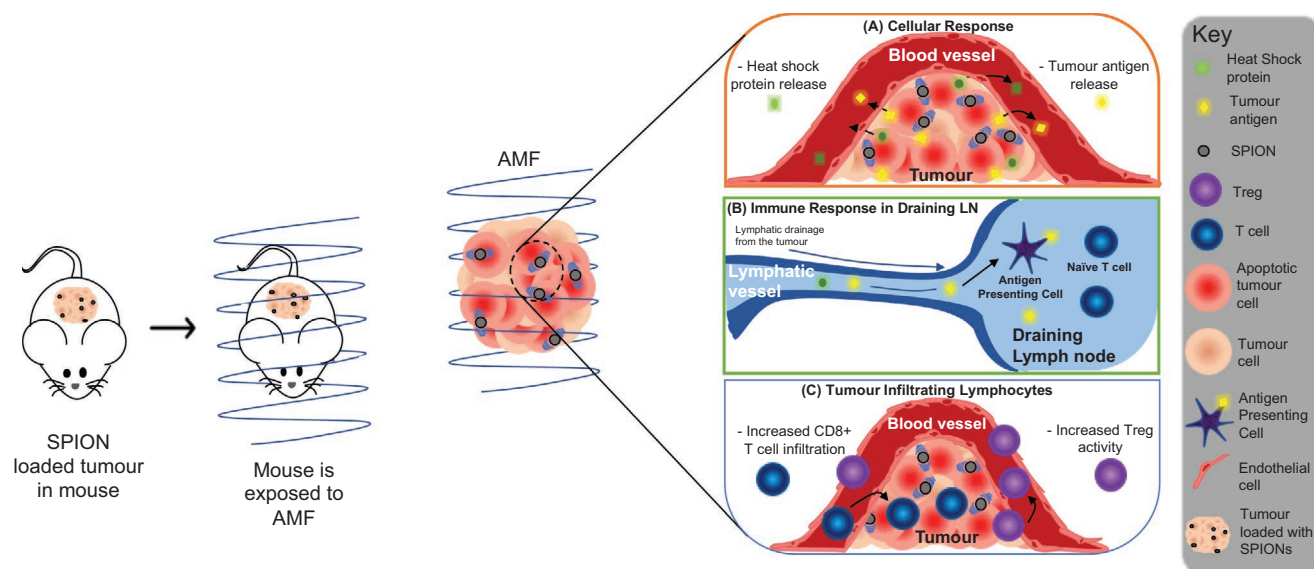Faculty of Pharmacy
The British University in Egypt (BUE)
El Shorouk City, Misr- Ismalia Desert Road, 11873 Cairo, Egypt
Dr. M. Shevtsov
Technical University of Munich
Klinikum Rechts der Isar, Ismaninger str. 22, Munich 81675, Germany

Intratumoral delivery of SPIONs is an exciting and viable option for targeted cancer MH. Previous preclinical studies have shown that SPIONs can achieve appropriate intratumoral distributions and can generate heat with no serious adverse effects.[35–37] Clinical studies in recurrent glioblastoma have demonstrated that intratumoral instillation of SPIONs with subsequent heating appears to be both safe and tolerable, resulting in favorable overall survival when compared to previous clinical trial populations.[36] Subsequent post-mortem investigations demonstrated that particles were restricted to the sites of injection and remained within the tumor following injection; predominantly within macrophages.[38] In this set of preclinical and clinical studies the authors speculated that the therapeutic effect was generated due to the induction of tumor necrosis upon application of hyperthermia.[35,37] However, the plausible effects on the tumor microenvironment, particularly the induction of anti-tumor immune responses, were not evaluated.

It is now thought that a key component of the therapeutic effect of hyperthermia is the induction of a heat-mediated immune response against the tumor,[39] enhancing the visibility of the tumor to the immune system (**Figure 1**). The increase in temperature leads to tumor antigen release by apoptosis and induces the expression of damage-associated molecular patterns, particularly heat shock proteins (HSPs).[40] HSPs have diverse functions; whilst intracellular HSPs protect against tissue injury by preventing apoptosis,[41] extracellular HSPs are involved in a number of immunological processes, including facilitating both the delivery of antigens to antigen presenting cells (APCs) and the expression of these antigens via major histocompatibility (MHC) proteins.[42–46] These processes could lead to the initiation of an anti-tumor T cell immune response, the induction of which could elicit long-term tumor control.[47] Thus, MH treatment offers the potential to achieve spatially- and temporally-controlled temperature increases, which may act as an immune trigger.[2]

In our study we investigated the heating ability and therapeutic potential of perimag-COOH, a dextran-coated SPION which possesses efficient heating ability compared to other, commercially available, similar SPIONs.[48] We conducted experiments to quantify localization of perimag-COOH within tumors and evaluate their fate following intratumoral injection. Once localization was established, a pre-clinical magnetic alternating current hyperthermia (MACH) system was used to generate an AMF capable of producing clinically relevant and measurable temperature increases in a subcutaneous in vivo syngeneic mouse model. To assess biological responses, digital image analysis of whole slide scans of heat-shock protein 70 (hsp70) expression was performed, alongside characterization of tumor infiltrating lymphocyte populations, to look for evidence of an anti-tumor immune response following MH treatment.

2. Results and Discussion

2.1. In Vivo Fate of Perimag-COOH Following Intratumoral Injection

Perimag-COOH is a dextran coated, negatively charged SPION with a hydrodynamic diameter of ≈130 nm. Assessment of the

Figure 1. Schematic figure showing the experimental layout and the proposed immunological and tissue responses to SPION-mediated hyperthermia therapy.

magnetic and heating properties (Supporting Information; Hyperthermic Potential of Perimag-COOH) confirmed that perimag-COOH possesses potential to generate MH (Figure S1, Table S1, Supporting Information). Using the syngeneic GL261 murine model of glioma, we tested if perimag-COOH SPIONs could be injected directly into subcutaneous tumors and retained in sufficient quantities to generate localized hyperthermia in vivo. SPION injection volume was calculated based on the theory that a given volume of SPION solution will distribute into an area approximately three times its volume.[49] Tumors were injected when they reached a volume >50 mm³ and the injection volume of 0.34 µL per mm³ of tumor tissue was capped at 100 µL, that is, any tumors >300 mm³ received an injection volume of 100 µL. Animals were sacrificed twenty-four hours following injection, at which point tumors were surgically excised, prepared for histological analysis and stained using Prussian blue (Perls) and hematoxylin and eosin (H&E). Results from these experiments (**Figure 2**A) showed that SPIONs were visible in tumors using both staining methods. SPIONs were visualized as blue staining (Perls) indicating the presence of iron and also as golden-brown patches of iron on H&E stained tissues. SPIONs were found to be confined mainly to the necrotic tumor regions and the tumor capsule.

In order to quantify the intratumoral retention of perimag-COOH SPIONs within GL261 tumors, systemic biodistribution studies were performed, utilizing perimag-COOH SPIONs radiolabeled at the iron oxide core using Zirconium-89 (^{89}Zr) as described previously.[30,50] ^{89}Zr-perimag-COOH was administered in an injection volume of 0.34 µL mm⁻³ tumor volume. Injected mice were then imaged using positron emission tomography/computed tomography (PET/CT) at 1, 24, 48, and 72 h following injection (n = 4). Representative images from a single animal at all time points (Figure 2B) clearly show that the signal was localized within, or around the tumor (injection

site) at all time points. Ex vivo organ counting was conducted at 24, 48, and 72 h following injection (n = 3 per group). Results confirmed that the majority of the injected dose (ID) was present either within the tumor, or within the skin and tissue overlying the tumor (Figure 2C). On average across all time points, 49% of the ID was retained within the tumor (21–87%, n = 9). At 72 h post injection, 46% was retained (36–57%, n = 3). Some uptake within the liver was observed (1.8 %ID ± 0.6 %ID at 24 h, 2.3 %ID ± 2.0 %ID at 48 h, and 4.2 %ID ± 3.4 %ID at 72 h) suggesting a percentage of SPIONs tracking to this organ via the blood. When organ uptake was compared using tumor:tissue ratios per gram of each tissue, tumors were found to have 3–5× more ID of SPIONs per gram of tissue than the skin overlying tumor, and over 50× more ID per gram than any other tissue analyzed.

When the thresholding of the PET images was altered, uptake was visible within tumor draining lymph nodes (LNs) at all time points studied, up to 72 h (Figure 2D; Left). Between all mice, lymphatic uptake was observed at focal points consistent with inguinal, axillary, para-aortic, and mediastinal LNs. To confirm that these signals represented the presence of perimag-COOH SPIONs and not free-^{89}Zr, inguinal LNs and tumors were dissected following the 72-h time point scan and fixed for histological analysis. Following radioactive decay, tumors and LNs were stained using Perls to confirm the presence of SPIONs (blue staining) in tumors injected with perimag-COOH SPIONs (Figure 2D; Right). Blue staining was also visible within the ipsilateral LN, but absent within the contralateral inguinal LN, reflecting the tracking of perimag-COOH to tumor draining LNs. To quantify perimag-COOH uptake within these LNs, PET image analysis was conducted to establish the changes in the %ID present within draining LNs. Results, shown in Figure 2E, demonstrate that the estimated %ID present in and around tumors fell to between 70% and 80% over time, with a corresponding increase in %ID within draining

ADVANCED
SCIENCE NEWS
www.advancedsciencenews.com

NANO · MICRO
small
www.small-journal.com
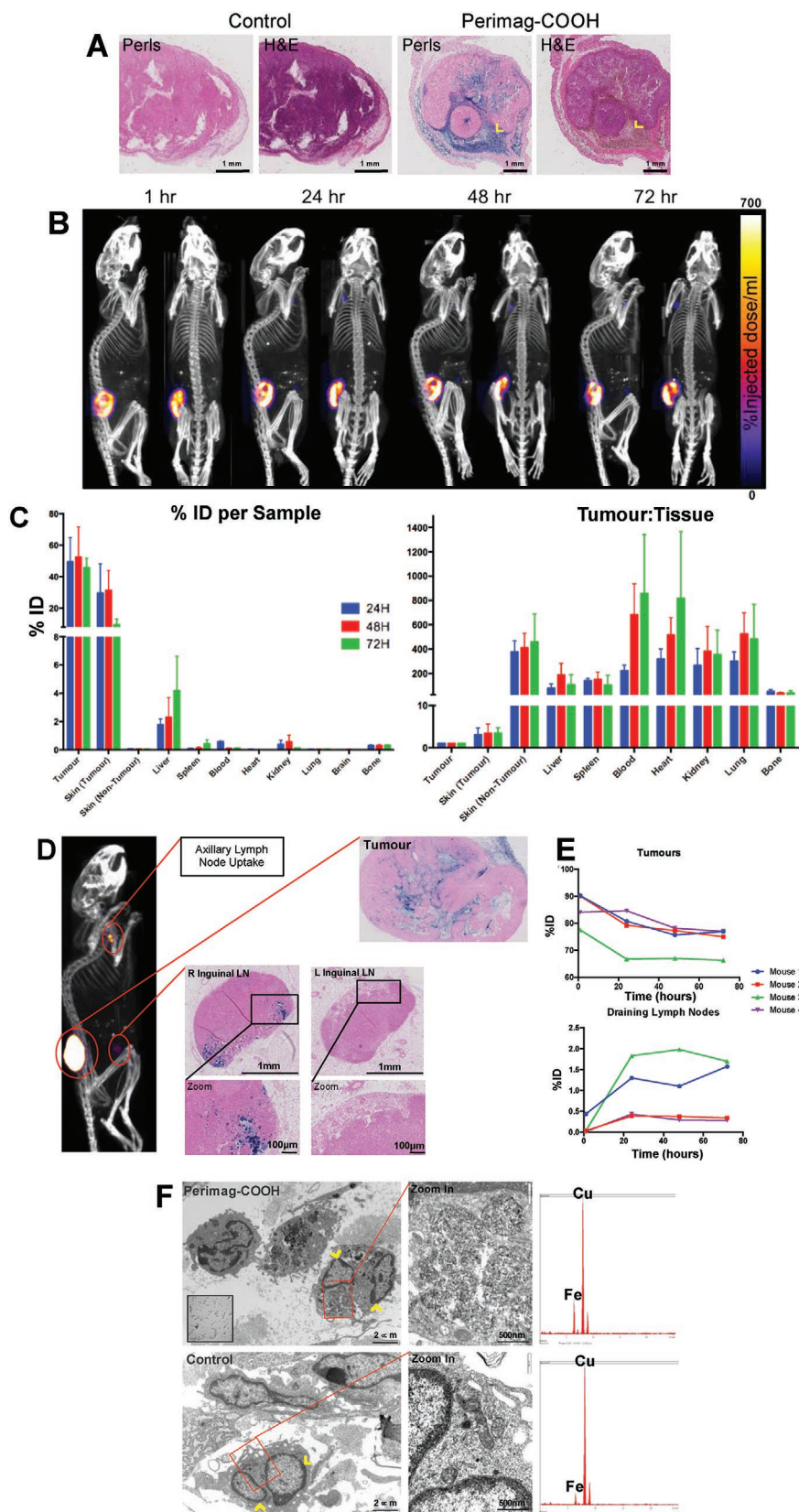
Figure 2. In vivo fate of perimag-COOH following intratumoral injection. A) Intratumoral distribution of perimag-COOH assessed histologically 24 h following direct intratumoral injection using Prussian blue and hematoxylin and eosin (H&E) staining. SPIONs were seen within tumor tissue but mainly found within necrotic tumor regions and around the tumor capsule, appearing blue in Prussian blue stained sections and golden-brown

LNs up to between 0.5% and 2% over 72 h. Whilst PET image analysis is less accurate than ex vivo organ counting, results indicate that the majority of the SPIONs remained within and around the tumors, with only minimal loss via lymphatic drainage, for the 72 h studied.

Finally, to assess the distribution patterns of perimag-COOH within tumors in more detail, transition electron microscopy (TEM) was conducted (Figure 2F). These images confirmed the presence of SPIONS within tumors, visible as electron dense structures surrounded by dextran. Images also demonstrated that the majority of cellular uptake was by tumor associated macrophages within necrotic tumor regions; identified on micrographs by the presence of distinctive ellipsoidal nuclei.[51] These TEM findings are in keeping with post-mortem studies of patients who received intratumoral injections of aminosilane-coated SPIONs.[38] To confirm the rod-shaped structures did represent SPIONs, X-ray microanalysis was conducted (Figure 2F; right), showing that these structures possessed a high elemental iron (Fe) content, consistent with the assumption that they were SPIONs.

2.2. Magnetic Properties of Perimag-COOH SPIONs Following Intratumoral Injection

To assess whether the perimag-COOH SPIONs retained their superparamagnetic properties within tumors, biodistribution experiments were carried out using a previously described experimental technique which tests the nonlinear longitudinal responses (NLR) of SPIONs to a weak ac magnetic field.[52,53] NLR registers the second harmonic of magnetization (M_2) in the longitudinal geometry of the ac magnetic field and possesses a high sensitivity to the presence of superparamagnetic species in a sample, thanks to their unique magnetization dynamics. In the megahertz frequency range, superparamagnetic particles with magnetic moments between $\approx 10^3$ and 10^6 μ_B generate an appreciable NLR within small magnetic fields, especially pronounced in the order ≈ 10–100 Oe.[54] This approximately corresponds to the inflection point of the hysteresis loop ($M(H)$ curve), allowing a quantitative measure of the superparamagnetic material, in this case perimag-COOH, in a given tissue sample.[52]

To conduct measurements, perimag-COOH was injected directly into GL261 tumors as before, animals were sacrificed
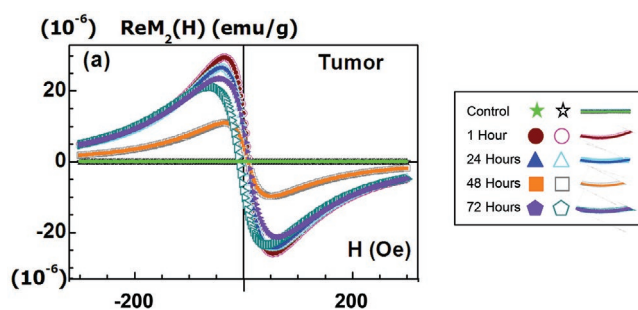
Figure 3. Non-linear magnetic response biodistribution. Biodistribution of perimag-COOH SPIONs in tumor tissue from the data on M_2 response (peak-to-peak/2 value of Re$M_2(H)$ in extremes (10^{-8} emu g^{-1}) is proportional to perimag-COOH concentration and the Im$M_2(H)$ component of response reflects the dynamical characteristics. Following intratumoral injection, animals were sacrificed at set time points and tumors were analyzed for SPION content. Larger magnetic moments were observed at the earliest time point (1 h) when compared with later time points (24, 48, and 72 h). Solid symbols represent direct H-scans, and open symbols represent reverse H-scans.[52,53] Full tabulated data can be found in Table S4, Supporting Information, with representative data from one animal per time point shown in Figure S1, Supporting Information.

at pre-determined time points (1, 24, 48, and 72 h post injection, $n = 3$ per time point). Tumors and selected other organs were dissected and analyzed for the presence of SPIONs by assessing the presence of superparamagnetic particles. Representative results showing the amplitudes from one animal at each time point are shown in Figure S2, Supporting Information, with average tumor data ($n = 3$ per time point) shown in **Figure 3**. These results suggest that perimag-COOH SPIONs retained their superparamagnetism following injection and were detectable within tumor tissue and the skin overlying tumors at all time points studied, consistent with the results found using ^{89}Zr-perimag-COOH (Figure 2). At the 24-h time point, SPIONs were also observed within liver and spleen tissue of the selected animal, likely representing SPION escape into systemic circulation following injection in this individual animal (Figure S2, Supporting Information). When the relative size of the magnetic moment within tumors at different time points was examined (Figure 3), it was noted that higher readings were obtained 1 and 24 h after injection (2778 ± 1814 and 2581 ± 2365 emu g^{-1}, respectively) compared with samples analyzed 48 and 72 h following injection

in H&E stained sections as indicated by the yellow chevron. B) Animals were injected with ^{89}Zr-perimag-COOH and imaged using PET-CT at 1, 24, 48, and 72 h following injection. The majority of the injected dose was visualized at all time points in and around the tumor with minimal uptake elsewhere. Threshold settings HU = −100–3500, %ID g^{-1} 0–700. C) Ex vivo organ counting was conducted at 24, 48, and 72 h following injection ($n = 3$). At all times studied, the majority of the injected dose (ID) was seen either in the tumor, or in the skin overlying the tumor, with minimal uptake in liver, spleen, and bone. Data are represented as percentage of injected dose per organ sample (%ID/T; left) and as a ratio of tumor:tissue of injected dose per gram of tissue (%ID g^{-1}; right). Error bars represent standard error of the mean. D) When the thresholding of the PET image at 24 h was altered, uptake originally masked by signal in the tumor was identified in ipsilateral axillary and inguinal lymph nodes (LNs) (image shown from 72 h time point). Prussian staining of tumor and ipsilateral draining inguinal LN confirmed the presence of perimag-COOH, whilst SPIONs were absent from the contralateral LN. E) PET/CT quantification of the percentage of injected dose (%ID) present at the injection site (tumor) and in visible lymph nodes at all imaged time points. F) TEM was conducted on GL261 tumors 24 h following intratumoral injection, confirming the presence of perimag-COOH SPIONs within macrophages (nuclei highlighted using yellow chevrons). SPIONs appear as electron dense rod-shaped structures surrounded by less electron-dense dextran (inset: TEM image of perimag-COOH alone). Following identification of SPIONs, samples were analyzed using X-ray microanalysis. Results confirmed the presence of a large iron (Fe) peak in samples containing perimag-COOH, compared to control tumors where a much smaller iron peak was visible. The large peak present in both images corresponds to elemental copper (Cu) from the grid upon which tissue samples were mounted. Full organ data can be found in Tables S2 and S3, Supporting Information.

(1040 ± 454 and 2246 ± 296 emu g^{-1}, respectively) (Table S4, Supporting Information). The high error measurements, as well as the finding that measurements are lowest at the 48-htime point, likely reflect the small sample sizes and variability in SPION content between the tissue samples chosen for analysis. These results suggest that SPIONs retained within the tumor at these later time points either possess less superparamagnetic activity or are present in smaller quantities; as similarly shown using ^{89}Zr-perimag-COOH, where the PET image reconstruction demonstrated a gradual fall in tumor SPION content over the first 24 h with a subsequent stabilization at 72 h (Figure 2E).

To be suitable for use in MH therapy, it is vital that SPIONs retain their superparamagnetic heat-generating properties. Following implantation, SPIONs are known to degrade very slowly over a period of up to 6 months, and remain visible on MRI throughout this time, with no discernible toxic effects.[55] Furthermore, post-mortem studies on patients with glioblastoma who underwent intratumoral SPION injection have revealed the presence of SPIONs within macrophages in tumors, months following implantation.[38] On a cellular level, cell division and exocytosis are the two main mechanisms which can dilute the quantity of SPIONs present inside a given cell[56] with studies suggesting that exocytosis occurs more rapidly for smaller sized particles,[57] and that SPIONs and the iron oxide contained within them are degraded over time via physiological iron metabolism pathways.[58] In summary, testing the NLR of perimag-COOH following injection into subcutaneous GL261 tumors, show that the SPIONs retain their superparamagnetic properties in vivo over a suitable time period for use in MH experiments.

2.3. Generation of Tumor Restricted Hyperthermia and Tumor Growth Response to Hyperthermia
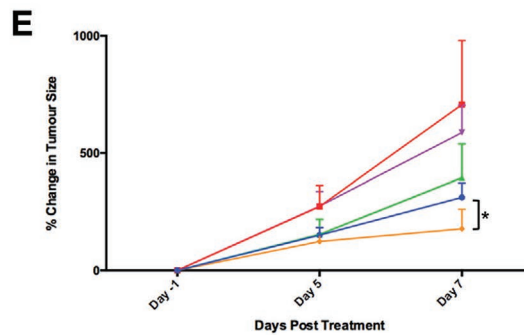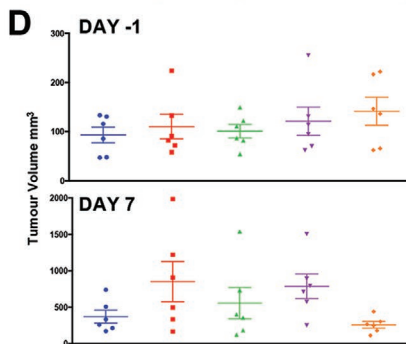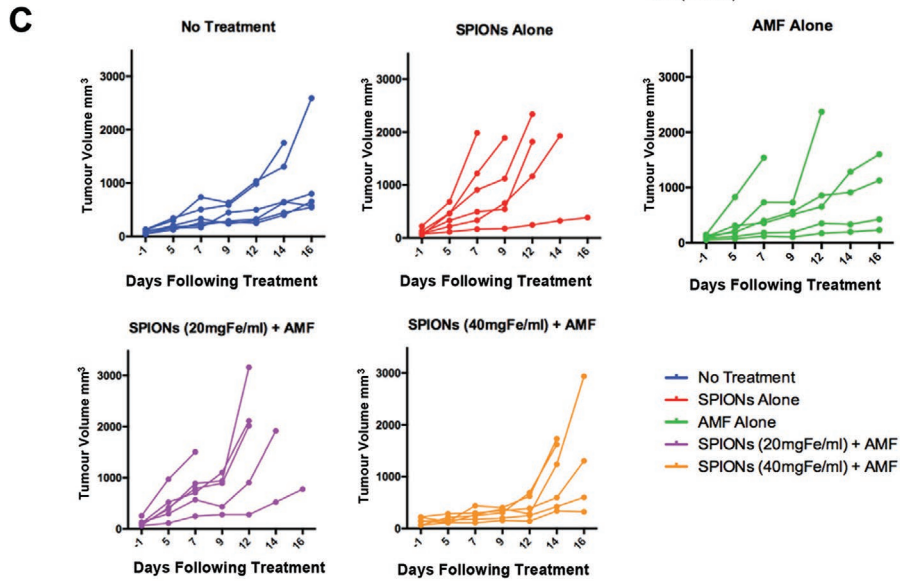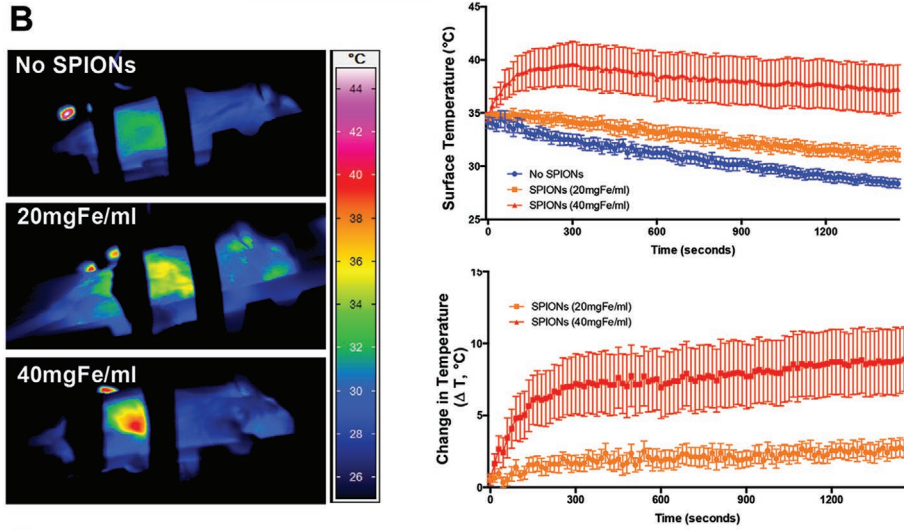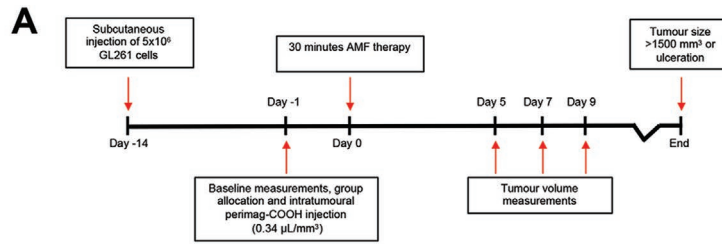
Following our observations that superparamagnetic perimag-COOH SPIONs appear to remain within tumors for up to 72 h following injection, experiments were designed to evaluate whether perimag-COOH could generate relevant temperatures when injected into GL261 tumors and exposed to an AMF. We adapted published protocols[59–61] to use a single AMF exposure. Tumors were injected as described previously once >50 mm^3 and exposed to an AMF for 30 min, via the purpose-built pre-clinical MACH system (Resonant Circuits Limited, London), 24 h following injection. Two perimag-COOH concentrations were used (20 and 40 mg$_{Fe}$ mL^{-1}) which at 0.34 µL mm^{-3} corresponded to 0.68 and 1.36 mg$_{Fe}$ per 100 mm^3 tumor tissue, respectively. Temperature monitoring during treatment was conducted using a thermal camera. The results, shown in **Figure 4** indicate that intratumorally administered perimag-COOH SPIONs generated tumor surface temperature increases of up to 5 °C above baseline, whilst tumors exposed to 30 min of an external AMF without perimag-COOH demonstrated no skin surface heating, and in fact underwent normal anesthetic-driven physiological cooling during the treatment. The resulting temperature difference between treated and untreated tumors after 30 min was up to 9 °C. As intratumoral temperature monitoring was not possible, skin temperature was
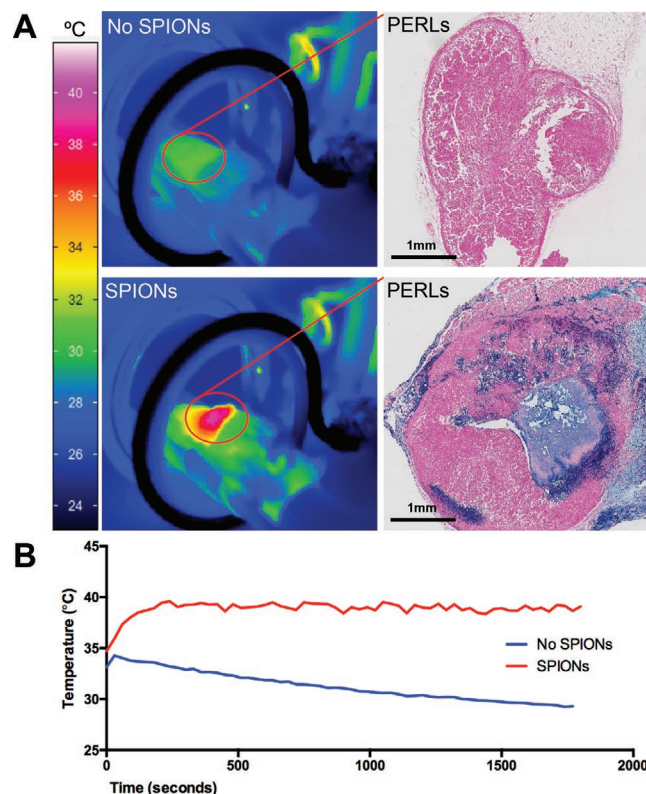
Figure 4. Representative example of in vivo heating ability of perimag-COOH. A) Two GL261-tumor bearing mice were selected. One mouse received no intratumoral injection, whilst the second mouse received an intratumoral injection of perimag-COOH SPIONs (0.34 µL mm^{-3}; tumor volume 285 mm^3; 95 µL, 40 mg$_{Fe}$ mL^{-1}). B) Following MACH therapy, thermal camera data were extrapolated into temperature curves. For those tumors injected with perimag-COOH SPIONs, skin surface temperatures up to 40 °C were observed, whilst in control tumors, surface temperatures gradually reduced over time, in keeping with normal physiology under anesthetic.

taken as an approximate reflection of internal tumor temperature. Following MH treatment, tumors were dissected and stained using Prussian blue confirming the presence of perimag-COOH SPIONs within tumors with elevated skin surface temperatures; no SPIONs were detected in non-heating tumors (Figure 4A). When thermal imaging data were plotted as temperature curves (Figure 4B), sustained surface heating of SPION-containing tumors was observed for the duration of treatment.

Next, we assessed the biological response and the potential therapeutic effects of intratumoral MH therapy. Previously used methods to evaluate the efficacy of MH include tumor growth analysis and survival,[59,61,62] analysis of apoptosis in histological samples,[59] histological analysis of tissue necrosis,[35,60,61] and immunohistochemical (IHC) analysis of tumor proliferation.[35] We first evaluated the response to treatment by measuring tumor growth following MH therapy with perimag-COOH at 20 mg$_{Fe}$ mL^{-1} ($n = 6$) or 40 mg$_{Fe}$ mL^{-1} ($n = 6$). The tumor growth rates of these two groups was compared to tumors injected with perimag-COOH SPIONs (20 mg$_{Fe}$ mL^{-1}) alone with no AMF exposure ($n = 6$), AMF exposure alone ($n = 6$), and untreated controls ($n = 6$). As before, tumor surface temperature was

ADVANCED
SCIENCE NEWS

www.advancedsciencenews.com

NANO · MICRO
small
www.small-journal.com

monitored throughout treatment using thermal imaging and extrapolated into heating curves to show absolute skin surface temperatures and changes in temperature, compared to control tumors (**Figure 5**A). These heating curves demonstrated that higher tumor surface temperatures were observed at both dose concentrations when compared with controls, but only animals treated with perimag-COOH SPIONs at 40 mg_{Fe} mL^{-1} showed substantially higher tumor surface temperatures over the duration of treatment; the skin surface temperatures of tumors injected with perimag-COOH SPIONs at 20 mg_{Fe} mL^{-1} fell slowly throughout treatment.

Size measurements were taken for all tumors in all groups at pre-set time points; the day before AMF exposure, immediately prior to SPION injection (day-1), 5 days following AMF exposure (day 5), and then 3 times per week beginning at day 7. Results up to 16 days after AMF exposure showed that, whilst all tumors grew during this time frame, tumors injected with perimag-COOH at a concentration of 40 mg_{Fe} mL^{-1} and exposed to AMF appeared to have a slower growth than other groups (Figure 5B). To demonstrate this more clearly, individual tumor volumes for each animal in each group were compared at day-1 (pre-treatment) and day 7 following treatment (Figure 5C), which showed that the tumors treated at 40 mg_{Fe} mL^{-1} were consistently smaller compared with other groups. When the percentage growth of each tumor from baseline was calculated on day 5 and 7 post-AMF exposure; the last time point at which all animals remained alive, a trend toward slower growth rates was observed in animals injected with SPIONs at 40 mg_{Fe} mL^{-1} (Figure 5D) ($p = 0.05$ at day 7, when compared to the no treatment group using a 2-tailed t-test assuming unequal variance). No effects from AMF exposure were observed in animals injected with SPIONs at 20 mg_{Fe} mL^{-1}.

2.4. Evaluation of Intratumoral Heating by Spatial Visualization of Hsp70 Expression

To evaluate whether the reduction in tumor growth observed following MH therapy was associated with histologically measurable changes, the expression of the 70 kDa heat shock protein, hsp70, was assessed in GL261 tumors treated with MH therapy at 3 time points following treatment; 1 h ($n = 4$), 24 h ($n = 4$), and 48 h ($n = 4$). Hsp70 was chosen due to its well characterized role as a cellular stress marker. HSPs, including hsp70, play complex roles in protein homeostasis,

including preventing protein aggregation and facilitating protein folding. Furthermore, there is emerging evidence that some HSPs may be involved in malignant processes including proliferation, invasion and metastasis,[63] and in the adaptive immune response as molecular chaperones, trafficking antigens to APCs, and facilitating antigen presentation via MHC proteins.[64,65]

Representative histological sections stained for hsp70 are shown in **Figure 6**A and appear to show increased hsp70 expression in tumors analyzed 24 and 48 h following treatment. To provide quantitative values for this result, we performed digital image analysis on whole slide images. The aims of this analysis were to identify both SPIONs and hsp70 positive cells within tumor sections and evaluate i) the proportion of hsp70 positive cells and ii) the spatial relationship between hsp70 positive cells and perimag-COOH SPIONs in the tumor sections. To develop initial image analysis protocols, tumor sections stained for the presence of cleaved-caspase 3 were used because of its predictable expression pattern around the edges of the necrotic tumor regions. First, protocols were designed to automatically differentiate SPIONs from positive cells, by isolating nuclei (blue; hematoxylin), positive cells (pink; stained red using Ventana RedMap kit) and SPIONs (brown; natural color) (Figure S3, Supporting Information). Following this, digital image analysis software (Definiens Developer XD 2.6; Munich) was utilized to isolate viable tumor tissue from background tissue and necrotic tumor regions to eliminate necrotic and non-tumor tissue from analysis (Figure S4, Supporting Information). The final step utilized hsp70 stained samples to develop a protocol capable of determining the relationship between the presence of SPIONs in the tissue samples and the location of hsp70 positive cells, based on the tissue staining described above (Figure S5, Supporting Information). Methodology for digital image analysis is provided in Supporting Information methods. Analysis of hsp70 stained sections revealed that the proportion of hsp70 cells in tumors increased significantly over time reaching the highest point 48 h post treatment (Figure 6B) when evaluated using Pearson ($r = 0.48$, $p < 0.05$) and Spearman's rank ($r_s = 0.68$, $p < 0.001$) correlation coefficients. Moreover, hsp70 positive cells appeared to be spatially related to the presence of SPIONs within the tumors, with a greater proportion of hsp70 positive cells situated in close proximity to SPIONs within the tumor sections at the 24 and 48-h time points (Figure 6C).

The biological effects of hsp70 within tumors are complex and difficult to predict. Increased hsp70 expression following

Figure 5. Hyperthermia and tumor growth. A) Schematic experimental outline. B) Left: Representative thermal camera images from each experimental group exposed to AMF. From top to bottom; tumors not injected with SPIONs and exposed to AMF alone; tumors injected with perimag-COOH at a concentration of 20 mg_{Fe} mL^{-1} and exposed to AMF; tumors injected with perimag-COOH at a concentration of 40 mg_{Fe} mL^{-1} and exposed to AMF. Right: Top: Tumor surface temperatures for the three experimental groups exposed to AMF. Bottom: Change in surface temperature (ΔT) for tumors injected with perimag-COOH at concentrations of 20 and 40 mg_{Fe} mL^{-1} and exposed to AMF, compared with control samples. All curves represent the mean heating for all the mice in the group ($n = 6$), with error bars representing the standard error of the mean (SEM). C) Tumor growth rates for all groups presented as individual tumor volumes at set time points following AMF exposure, up to 16 days post treatment. Each line represents a separate tumor, and data are separated into respective groups ($n = 6$ per group). D) Tumor volumes for each individual animal measured at day 1 (before treatment; top) and day 7 (1 week following treatment; bottom) demonstrating the slower tumor growth of animals treated with MH using perimag-COOH at 40 mg_{Fe} mL^{-1}. E) Grouped tumor growth analysis represented as mean percentage (%) increase in tumor size from baseline up to seven days post treatment. Error bars represent SEM, $*p = 0.05$ when compared using the 2-tailed t-test assuming unequal variance.
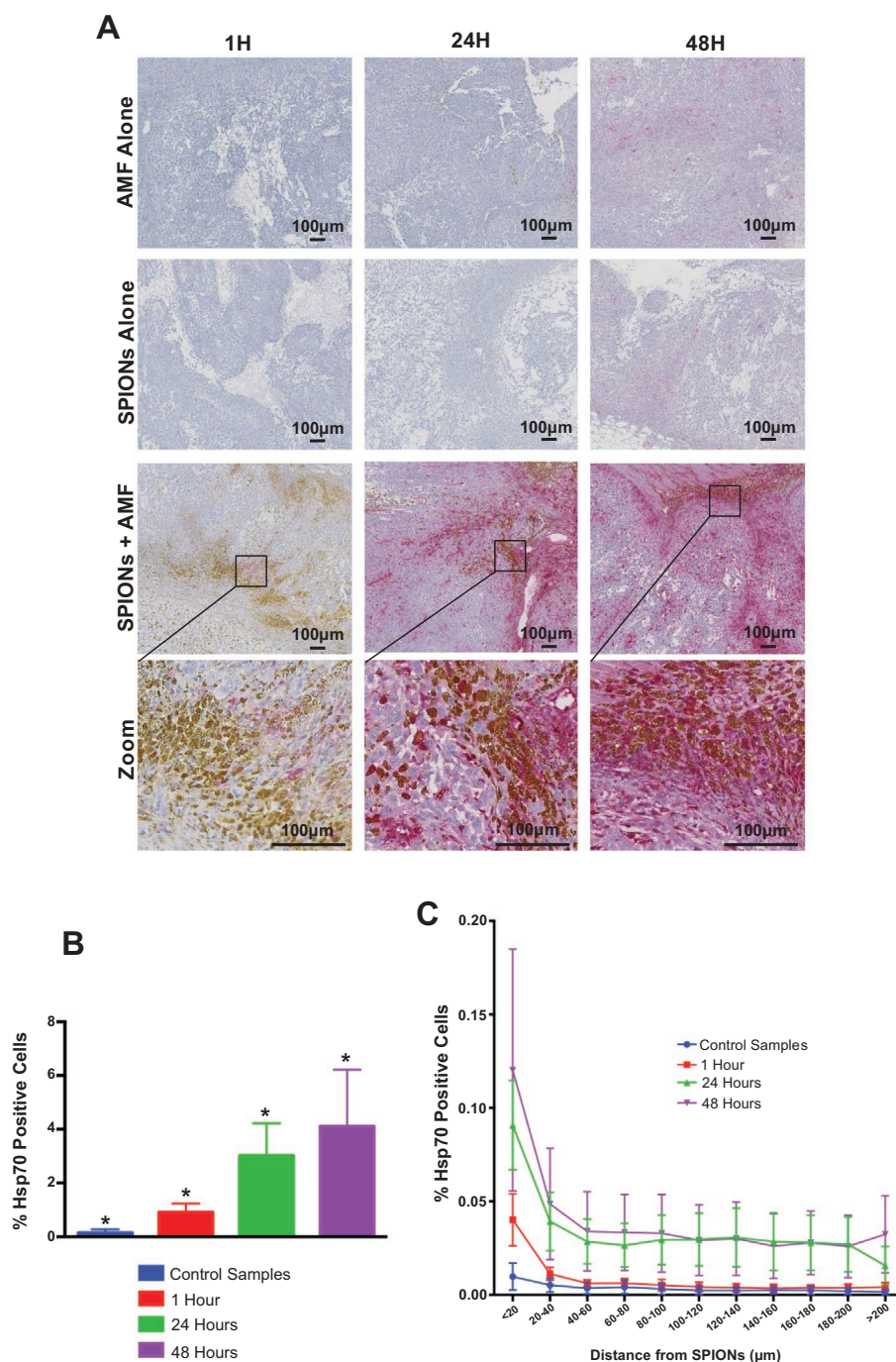
Figure 6. Hsp70 expression following magnetic hyperthermia. A) Representative examples of tumor sections stained for hsp70 from each experimental group and the SPION-only control group. In these sections, cell nuclei are stained blue, whilst cells that are positive for hsp70 appear red, and perimag-COOH SPIONs appear brown in color. B) Hsp70 staining was higher than grouped controls at all studied time points, increasing up to 48 h, the latest time point studied. *Correlation of hsp70 expression and time following MACH therapy was found to be statistically significant when analyzed using Pearson ($p = 0.02$, $r = 0.48$) and Spearman's rank ($p = 0.0004$, $r = 0.68$) correlation coefficients. C) Digital image analysis was conducted using Definiens Developer XD. When hsp70 staining was compared to the presence of SPIONs, results indicate a relationship between the presence of perimag-COOH within the tumors and the expression of hsp70. Error bars represent SEM.

MH could protect the tumor from the hyperthermia,[66] but may also indicate a process of immunomodulation, which could generate an anti-tumor immune response,[67,68] including influx and activation of cytotoxic (CD8+) T cells.[69] In summary, increased hsp70 expression, combined with apparent slowing of tumor growth following MH therapy is indicative of changes within the tumor microenvironment, warranting further investigation.

ADVANCED
SCIENCE NEWS
www.advancedsciencenews.com

NANO · MICRO
small
www.small-journal.com

2.5. Characterizing Changes in the Tumor Immune Landscape Following Hyperthermia

Flow cytometry analysis was utilized to evaluate whether increased hsp70 expression within tumors following MH was associated with changes in the characteristics of the T cell populations within i) tumors and ii) sentinel draining LNs. Experiments were designed as outlined in **Figure 7**A with GL261 tumors implanted on both flanks of C57BL/6 mice. Once >50 mm³, tumors on the left flank received an injection of perimag-COOH SPIONs (40 mg_{Fe} mL^{-1}), whilst tumors of the right flank were not injected with perimag-COOH. After 24 h, all tumors were subjected to 30 min of AMF exposure, allowing for paired analysis of results. As before, skin-surface temperature was monitored and recorded (Figure 7B), demonstrating that tumors injected with perimag-COOH SPIONs ($n = 5$) showed consistently higher maximum surface temperatures (T_{max}) than their corresponding untreated paired control tumors ($n = 5$). Seventy-two hours following MH therapy, tumors and their corresponding draining inguinal LN were harvested, digested, and processed to isolate T-lymphocytes. The time point of 72 h following MH therapy was selected to capture early changes in both tumor infiltrating lymphocyte (TIL) populations and T cells in draining LNs, without allowing time for a systemic immune response, thus negating the possibility of an abscopal immune response in the contralateral tumor,[70] as has been observed in other studies.[71] Resulting tumor and LN cell samples were stained and characterized using flow cytometry to isolate and compare the populations of CD8+ and CD4+ T cells present.

To analyze the TILs, the percentage of both CD4+ and CD8+ T cells in each treated tumor were compared to the percentages in each respective untreated control tumor. In order to isolate CD8+ and CD4+ T-cells, cells were positively selected for CD45 (a hematopoietic cell marker) and CD3 (a mature T-cell marker) and negatively selected for CD11b (a marker of non-T-cell hematopoietic cells such as macrophages). These results showed a clear trend toward an increased proportion of cytotoxic CD8+ T cells, with a corresponding reduction in the proportion of CD4+ helper T cells, in tumors treated with MH (**Figure** 8A). Interestingly, clinical studies in cancer patients have reported that increased tumor infiltration of CD8+ cytotoxic T cells can represent a positive prognostic factor.[72]

When the CD8+ and CD4+ TIL populations were analyzed in more detail, a higher proportion of the CD4+ TILs within treated tumors were found to be positive for the regulatory T cell (T-reg) marker FoxP3+ (Figure 8B), suggesting a greater proportion of T-regs were present. Furthermore, of those FoxP3+ CD4+ T cells present, a significantly higher proportion were found to be Ki-67+ ($p = 0.03$), suggesting that these T-regs were actively proliferating, which could contribute to immunosuppression within the tumors. There are suggestions that a corresponding increase in T-regs following CD8+ infiltration may in fact be driven by the CD8+ T cells themselves, as part of a negative feedback loop reaction.[73,74]

Within the CD8+ TILs (Figure 8C), a significantly greater proportion were shown to express PD-1 ($p = 0.004$), which can either represent a marker of activation at moderate expression levels, or of T cell exhaustion when expressed at higher levels.[75] There is also evidence that tumor-infiltrating CD8+ T cells that express PD-1 may be functionally impaired despite demonstrating specificity for tumor antigens.[76] CD8+ cells also showed high Ki-67 expression; reflective of increased proliferation ($p = 0.001$), and higher expression of the serine protease granzyme B, which is commonly found in the vesicles of cytotoxic T cells and is suggestive of increased killing ability ($p = 0.008$) (Figure 8D). The mean fluorescence intensity of this granzyme B expression was measured and shown to be significantly higher in CD8+ TILs extracted from treated tumors compared with matched untreated controls ($p = 0.02$); suggesting that a greater proportion of granzyme B was present within the CD8+ T cells in tumors treated with MH.
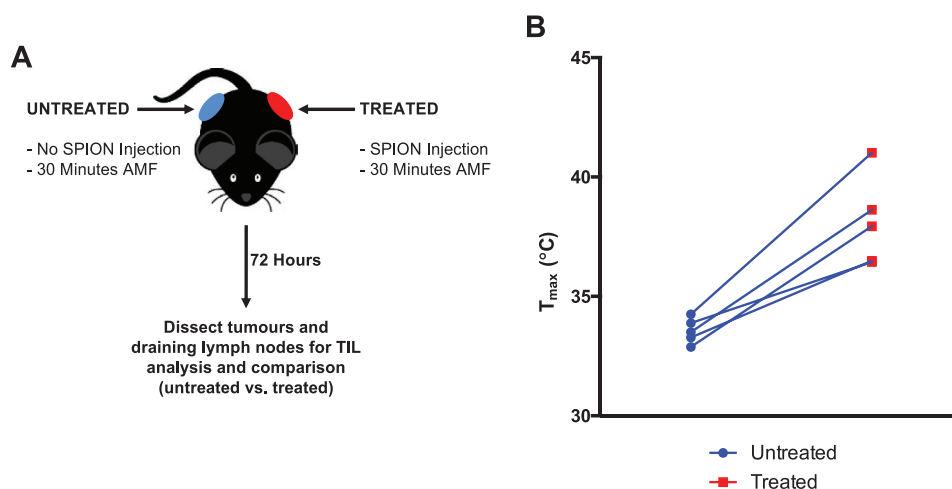
Figure 7. Experimental set-up for analysis of tumor infiltrating lymphocyte (TIL) populations. A) Schematic representation of the experimental set-up for analysis of the tumor infiltrating lymphocyte populations in subcutaneous GL261 tumors. B) Skin surface temperatures monitored using thermal imaging. During magnetic hyperthermia therapy, maximum recorded temperatures (T_{max}) were noted; temperatures overlying treated tumors (red) was consistently higher than those overlying untreated matched controls (blue).
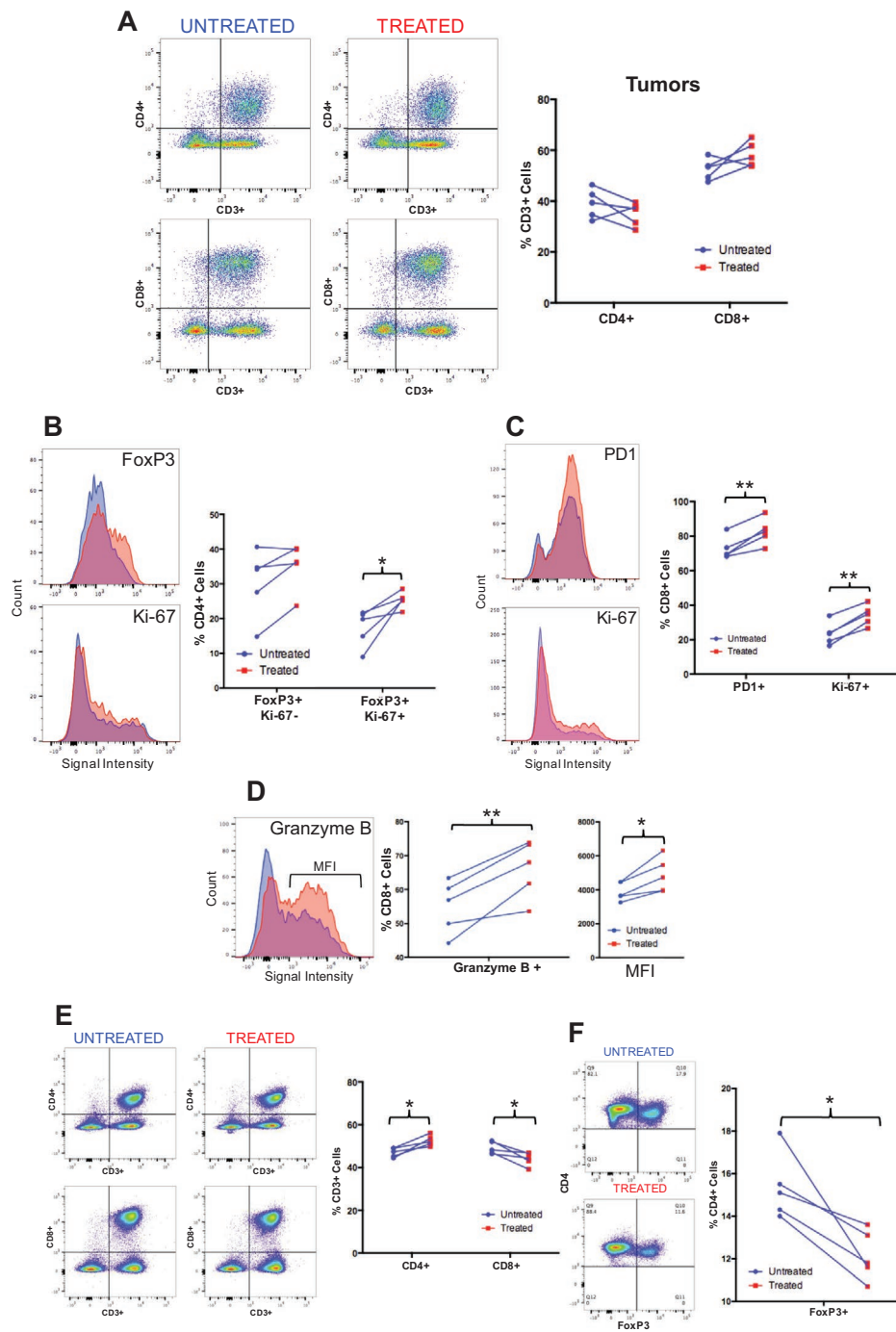
Figure 8. Flow cytometry analysis of T cell populations following magnetic hyperthermia. A) Left: Representative plots of CD4+ (top) and CD8+ (bottom) T cells gated on CD45+, CD11b−, CD3+ cells isolated from subcutaneous GL261 tumors 72 h following MH therapy. Right: Group analyses demonstrating that there was a pattern toward a decrease in the proportion of CD4+ T cells following treatment and an increase in the proportion of CD8+ T cells. B) Analysis of the regulatory CD4+ T cells present within tumors following MH therapy. Left: Representative histogram of FoxP3 expression in CD4+ cells (top), and Ki-67 expression in FoxP3+ T cells (bottom) in an untreated (blue) and treated (red) tumor. Right: A higher proportion of CD4+ T cells are regulatory (FoxP3+) and proliferating (Ki-67+) within treated tumors ($n = 5$), compared to non-treated tumors ($n = 5$). C) Characteristics of the CD8+ T cells present within tumors following MH therapy. Left: Histogram representation of PD1 and Ki-67 expression of CD8+ TILs in an untreated (blue) and treated (red) tumor. Right: Grouped analyses showing that a significantly larger proportion of CD8+ T cells within treated tumors ($n = 5$) are activated (PD1+), and proliferating (Ki-67+). D) Granzyme B expression of CD8+ TILs in an untreated (blue) and treated (red) tumor. A significantly higher proportion of CD8+ cells within treated tumors are capable of killing (Granzyme B+) when compared with paired controls ($n = 5$). Furthermore, of those cells which are granzyme B positive, the mean fluorescence intensity (MFI) of cells staining positive for granzyme B was significantly higher in treated tumors compared to matched controls. E) Left: Representative plots of CD4+ (top) and CD8+ (bottom) T cells gated on CD45+, CD11b−, and CD3+ cells isolated from draining LNs of untreated ($n = 5$) and treated ($n = 5$) GL261 tumors. Right: Group analyses demonstrating

We next investigated whether the changes in TIL populations within tumors following MH therapy were associated with complementary changes in the T cell populations present within draining LNs. For this, CD4+ and CD8+ T cells isolated from LN's were compared. The results of this experiment, shown in Figure 8E, indicated a consistent decrease in the proportion of CD8+ T cells ($p = 0.03$), with a corresponding increase in the proportion of CD4+ T cells ($p = 0.01$); an opposite shift to that observed in tumors. Furthermore, when CD4+ T cells were analyzed in greater detail, a significantly lower proportion of these were FoxP3+ in the draining LNs of treated tumors ($p = 0.02$), suggesting that fewer T-regs were present following treatment (Figure 8F). Within LNs, T-regs are known to suppress anti-tumor immune responses,[77] therefore a reduction in the proportion of T-regs within the tumor draining LNs could provide further evidence of positive immunomodulation following MH therapy.

In summary, characterization of lymphocyte populations within subcutaneous GL261 tumors and draining LNs after MH showed shifts in both CD4+ and CD8+ populations that were consistent with the hypothesis that MH can induce an immune response within tumors.

3. Conclusion

Localized cancer hyperthermia therapy is a relatively unexplored treatment with potential for application in different regimes including immune stimulation. SPION mediated MH remains the most clinically developed nanotechnology platform for delivery of controlled hyperthermia to tumors, compared with nanomaterial-mediated photothermal therapy and radiofrequency ablation hyperthermia;[78,79] both of which are mediated most often by AuNPs, carbon nanomaterials, or hybrid NPs. However, although promising, large-scale clinical translation of MH has been limited by a number of persistent challenges: most notably, difficulty in localizing SPIONs within tumors and targeting them to tumor cells in addition to limitations in monitoring and regulation of the target temperatures.[80] Traditionally, studies on MH have aimed for tumor eradication by heat, with target temperatures chosen to achieve this. Now, the focus is beginning to shift toward the immunomodulation effects of lower grade hyperthermia (39–45 °C) which can initiate a cell stress cascade known as the unfolded protein response,[81] in turn generating an immune response. However, the optimum temperatures needed to achieve these effects remain undefined.[82] Evidence that temperatures of 43 °C were able to elicit an anti-tumor CD8+ T cell response, whilst temperatures of 45 °C were not, in the same experimental system,[83] indicate that there may be a narrow target window required for effective immunomodulation. Monitoring the temperature throughout the tumor presents a further challenge, with single point thermometry and thermal imaging only providing estimates of actual temperatures,[80] as also observed in the present study.

Increasingly, focus is moving away from utilizing hyperthermia as an independent therapy and instead seeking to understand and exploit ways in which hyperthermia therapy can complement and augment existing anti-cancer therapies, including immunotherapy.[84–88] The research presented in our study supports the hypothesis that SPION-mediated MH can initiate immune changes within tumors in vivo and our observations form a platform for new investigations to elucidate the immune response to MH. Further experiments could include investigating the components of innate and adaptive immunities, longer-term changes and studying macrophage or monocyte populations; all of which are vital components of the immune landscape within tumors and in presentation of tumor antigens in draining LNs.[89] In addition, testing MH in combination with cyclophosphamide,[90,91] anti-CD25 agents,[92] or immune checkpoint inhibitors could favorably shift the balance between regulatory (T-reg) and effector (CD8+) cells and work synergistically with MH,[93] further building on work presented in this manuscript.

4. Experimental Section

Perimag-COOH was obtained from Micromod Partikeltechnologie GmbH.

In Vivo Experiments: All animal studies were approved by the UCL Biological Services Ethical Review Committee and licensed under the UK Home Office regulations and the Guidance for the Operation of Animals (Scientific Procedures) Act 1986 (Home Office, London, UK).

Subcutaneous Tumor Implantation in C57BL/6 Mice: GL261 glioma cells were grown in filtered Dulbecco's modified Eagle's medium (Gibco) supplemented with 10% fetal bovine serum (Gibco), and 1% sodium pyruvate until 80% confluent. Cells were detached using trypsin and counted before being re-suspended in sterile PBS at a concentration of 5×10^6 cells per 100 µL. Animals were anesthetized with 2% isoflurane and 100 µL of the cell suspension was injected into the right flank. Animals were monitored closely for any adverse signs following injection. Tumor growth was monitored and animals were used for experiments once the tumors were >50 mm³ in volume as measured using calipers (≈2–3 weeks post implantation). Tumor volume was calculated by multiplying the three tumor dimensions together and dividing by 2 to correct for the elliptical shape of the tumors.

Intratumoral Injection of Perimag-COOH SPIONs into Subcutaneous GL261 Tumors: Intratumoral injections were carried out in line with a previously described distribution theory.[49] In brief; tumors were measured using digital calipers and an estimate of tumor volume was made. Tumors were injected with SPIONs once they reached a minimum estimated volume of 50 mm³. Mice were anesthetized with 2% isoflurane and placed on their side on a covered surface. SPION injection volumes were prepared at 0.34 uL mm⁻³ of tumor and loaded into a syringe with a 26 G needle attached. The needle was advanced into the center of the

---

that for each paired LN sample, a reduction in the proportion of CD8+ T cells was observed ($p = 0.029$), with a corresponding increase in CD4+ T cells ($p = 0.012$). F) Lymph node Regulatory T cell analysis. Within the draining lymph nodes of treated tumors, a lower proportion of CD4+ FoxP3+ T cells were observed compared to the corresponding untreated tumor. Left: Representative example FoxP3 expression on CD4+ cells in the draining LNs of untreated (top) and treated (bottom) tumors (gated on CD45+, CD11b−, CD3+ cells). Right: Grouped analysis showing that for all paired samples, a significant reduction in the expression of FoxP3 was observed in treated samples. *$p < 0.05$ when measured using a paired two-tailed t-test. **$p < 0.01$ when measured using a paired two-tailed t-test.

tumor and the needle was secured in place using a specially adapted clamp-stand. SPIONs were injected over 2 min and the needle was left in place for a further two minutes before being removed slowly over one minute. Following injections, mice were monitored closely until fully recovered.

Histological Procedures: Iron oxide nanoparticles within the tumor tissue sections were located by staining with potassium ferrocyanide (Perls Prussian blue). Adjacent sections were stained with H&E. IHC staining for hsp70 was performed on a ROCHE Ventana Discovery XT instrument. Anti-hsp70 antibody (clone ab181606, Abcam) was used, and incubated 1:1000 for 1 h before being detected using swine anti-Rabbit (Dako, E0353). Detection kit used was Ventana RedMap Kit (760-123). For pre-treatment either Ventana CC1 (950-124), equivalent to EDTA buffer, or Ventana Ribo CC (760-107), equivalent to citrate buffer, was used. Staining was optimized using mouse testicular tissue as a positive control tissue (Figure S6, Supporting Information). Slides were counterstained with hematoxylin.

Visualization of Perimag-COOH SPIONs in GL261 Tumors Using Transmission Electron Microscopy: Twenty-four hours following intratumoral SPION injection, tumors were dissected, cut into small fragments no larger than 2 mm in each dimension and fixed in 1.5% glutaraldehyde/1% paraformaldehyde/PBS pH 7.4, for a minimum of 2 h, and stored at 4 °C until processing for TEM. Tumor fragments were then washed with two changes of phosphate buffer (Oxoid) and post-fixed with osmium tetroxide solution (1% osmium tetroxide (Analar BDH) + 1.5% potassium ferricyanide (BDH) in PBS (Oxoid)). Following this, the tumors were washed using several changes of distilled water to remove the osmium tetroxide and dehydrated using increasing alcohol concentrations of 30%, 50%, 70%, 90%, and 100%. After dehydration, the samples were left in 50% alcohol/50% Lemix (TAAB) epoxy resin mixture on a mixer overnight to infiltrate with resin. They were then placed in 100% Lemix resin for a minimum of 4 h, embedded in fresh Lemix Resin and polymerized at 70 °C overnight. Semi-thin (1 μm) sections were cut using glass knives on a Reichert-Jung Ultracut microtome, collected on glass microscope slides and stained using Toluidine Blue solution (1% Toluidine Blue (Raymond Lamb) with 0.2% Pyronin (Raymond Lamb) in 1% sodium tetraborate (Analar BDH)). Ultrathin sections were cut using a diamond knife (Diatome) and collected on 300 HS, 3.05 mm copper grids (Gilder). The ultrathin sections were stained using saturated alcoholic uranyl acetate (UA) (TAAB) for 5 min followed by Reynold's lead citrate, also for 5 min.

Confirmation of SPION Presence Using Energy Dispersive X-Ray Microanalysis: Samples were prepared as above but were not stained with UA or lead. The sections were viewed and photographed using a Philips CM120 transmission electron microscope fitted with EDAX DX-4 microanalytical system for X-ray microanalysis of the samples.

Radiolabeling of Perimag-COOH with Zirconium-89 (^{89}Zr): Radiolabeling of perimag-COOH with ^{89}Zr was performed as previously described.[30,50] Zr-oxalate (^{89}Zr^{4+} in 1 M oxalic acid, Perkin-Elmer) 15 μL, 28.5 MBq was added to an Eppendorf tube. Chelex-treated water (200 μL) was then added and the pH raised to 8 using 1 M Na_2CO_3 (aqueous). This step was performed cautiously as acid neutralization with Na_2CO_3 generates CO_2 gas and base must be added carefully to avoid loss of radioactivity. Chelex-treated water was again added (500 μL), followed by the addition of perimag-COOH (400 μL, 50 mg$_{Fe}$ mL^{-1}). The nanoparticle mixture was then vortexed briefly and subsequently incubated at 100 °C for 60 min. The reaction was then allowed to cool to room temperature, DTPA (50 μL, 10 mM (pH 7.5)) was added and the mixture left to stir at room temperature for 30 min. After that time, the mixture was purified using size exclusion chromatography (PD10 Sephadex, G25), (eluted with fractions of sterile saline) and the recovery was 57%. ^{89}Zr-perimag-COOH was diluted to a concentration of 20 mg$_{Fe}$ mL^{-1} using sterile saline for in vivo studies. DLS was conducted before and after labeling to ensure that the physical properties of perimag-COOH remained stable following labeling. Radiolabeled SPIONs were injected at 0.34 μL mm^{-3} tumor volume, with animals receiving 0.3–1 MBq depending on tumor size.

PET/CT Imaging: Following intratumoral injection of ^{89}Zr-perimag-COOH, C57BL/6 mice were imaged with PET/CT at pre-set time points. Mice were anesthetized with isoflurane (2% in oxygen) and placed on the preheated bed of the scanner (set at 38 °C). Whole body static PET scans were acquired using nanoScan PET/CT (Mediso, Budapest, Hungary) followed by CT image acquisition. PET images were acquired using 1–5 coincidence mode and recorded for 20 min. CT images were acquired using a 50 kV peak X-ray source and 300 ms exposure time in 720 projections with an acquisition time of 7 min. Respiration rate was monitored throughout the scan. PET images were reconstructed using Tera-TomoTM 3D PET reconstruction software (Mediso version 2.01). CT images were reconstructed in voxel size of $68 \times 68 \times 68$ mm^3 using Nucline software (Mediso version 2.01). Image analysis and 3D visualization were performed using VivoQuant software (InviCRO version 1.23patch3). 3D regions of interests (ROIs) were created for each animal and were quantified in term of %ID for each time point using VivoQuant software (InviCRO version 1.23patch3). Representative images were presented using %ID mL^{-1} as color scale after correcting for Zr^{89} decay by using the same software using Gaussian filtering of 0.8.

Digital Image Reconstruction for Analysis of Lymph Node Uptake: 3D ROI were created for tumor and visible LNs and were quantified in term of %ID for each time point using VivoQuant software (InviCRO version 1.23patch3). Representative images were presented using %ID/mL as color scale after correcting for Zr^{89} decay (www.radprocalculator.com/Decay.aspx) using Gaussian filtering of 0.8. For each tumor and corresponding LNs, %ID was calculated and plotted over time for each animal.

Ex Vivo Biodistribution Studies: Mice from the imaging studies were used for the biodistribution studies. Mice under anesthesia were culled by cervical dislocation and the organs of interest were harvested. Each sample was weighed and counted with a gamma counter (Wizard 2480 PerkinElmer), together with standards prepared from a sample of the radiolabeled SPIONs. The percent of ID per tissue sample was measured, and the ID per gram (%ID g^{-1}) of each tissue was calculated in order to calculate ratios.

Non-Linear Magnetic Response Biodistribution: SPION distribution within ex vivo tissue samples was assessed using nonlinear magnetic response on the M_2 in the longitudinal geometry of ac- and direct current (dc)- magnetic fields, $H(t) = H_0 + h_0 \sin \omega t$. The dc field H_0 was scanned back-and-forth symmetrically within ±300 Oe with the round-up cycles 0.125–4 s and with high representativity of 2048 H-points in each scan. The amplitude $h_0 = 13.8$ Oe of the ac field with the frequency $f = \omega/2\pi = 15.7$ MHz ensured the condition $M_2 \propto h_0^2$. Both real (Re$M_2(H)$) and imaginary (Im$M_2(H)$) components of the signal were simultaneously recorded as functions of the dc field at the room temperature region. Since the main contribution to the real part was provided by a nonlinearity of a sample magnetization curve $M(H)$, Re$M_2(H) \propto \partial^2 M/\partial H^2$,[53] its amplitude was $\propto N_{MNP}$—the amount of SPIONs in a sample. The latter allows study of SPION biodistribution using M_2 measurements.[52]

Magnetic Hyperthermia Therapy and Thermal Imaging: GL261 tumor bearing mice were injected with perimag-COOH SPIONs as outlined above once the tumors were at least 50 mm^3 in volume and subjected to AMF no sooner than 24 h following injection of SPIONs. Animals were anesthetized using 2% isoflurane and placed within a specially designed plastic bed before being introduced into the center of the MACH coil (a double coil with Helmholtz configuration to maintain field homogeneity over the volume of the mouse; Resonant Circuits Limited, London, UK). Mice were exposed to 30 min of AMF (frequency 692 kHz, field strength 4.5 kA m^{-1}) and monitored closely for any signs of distress. Following completion of AMF, mice were further monitored until fully recovered and skin temperature was estimated using a thermal camera.

Tumor Growth Analysis: Tumors were measured using digital calipers before treatment, and at set time points following treatment. Measurements were performed by the same individual, who was blinded to the groups or treatments individual animals had received. Approximate tumor volumes were calculated and plotted as individual values and for grouped analysis using Graphpad PRISM.

Digital Image Analysis of Hsp70 Response: Using slides stained using DAB-Red, digital image analysis was performed on digitized slides (Leica SCN 400) using Definiens Developer XD 2.6 (Definiens AG, Munich). Full, detailed methods and results from protocol optimization are provided in Supporting Information.

Extraction and Isolation of Tumor Infiltrating Lymphocytes: Tumors were harvested and transported in un-supplemented RPMI, on ice. Tumors then placed in a 6 cm plate with 1 mL of Liberase/DNAse, cut into small pieces with a scalpel and transferred to a 15 mL falcon tube. The suspension was then incubated for 30 min in a water bath (37 °C) before being passed through a 70 µm cell strainer into a 50 mL flacon tube. Undissolved chunks of tissue were mashed through the cell strainer using the wide end of a 1 mL plastic syringe. The cell strainer was washed with 5 mL un-supplemented RPMI and the single cell suspension transferred to a fresh 15 mL tube before centrifugation at 1500 rpm for 5 min at 4 °C. The resulting cell pellet was resuspended in 5 mL of complete RPMI. A glass Pasteur pipette was placed in the tube to load 3 mL of room temperature Histopaque-1119, which was then allowed to drain into the bottom of the tube and layer under the RPMI/cell suspension. The Pasteur pipette was carefully removed and the solution centrifuged at 700×g for 10 min with no brake. Using a 1000 µL pipettor, the buffy coat layer of cells was transferred from the Histopaque/RPMI interface to a clean 15 mL tube and topped up to 5 mL with complete RPMI. The buffy coat/RPMI suspension was centrifuged at 400 xg at 4 °C for 5 min and the cell pellet resuspended in the desired volume of FACS buffer (200 µL per FACS Panel).

Flow Cytometry Analysis of Tumor Infiltrating Lymphocyte Populations: Extracellular and intranuclear/intracellular antibody master mixes were made as outlined below in superblock (PBS, 2% FCS, 5% normal rat serum, 5% mouse serum, 5% rabbit serum, 25 µg mL^{-1} 2.4G2 anti-Fc receptor mAb, 0.1% sodium azide (NaN$_3$); Extracellular mastermix: anti-CD8 BV650 (clone 53–6.7, BioLegend, 100742, 1:300), anti-CD4 V500 (clone RM4-5, BD Bioscience 560783, 1:300), anti-CD11b BV711 (clone M1/70, BioLegend 101242, 1:200), anti-PD-1 PercP-eF710 (clone J43, eBioscience 46–9985, 1:200), anti-CD45 PECy7 (clone 30-F11, BD Bioscience 100742, 1:200), and live-dead stain APC-Cy7 (eBioscience, 1:1000); Intracellular mastermix: anti-Ki-67 eFluor450 (clone SolA15, eBioscience 48-5698-80, 1:100), anti-CD3 BV785 (clone 17A2, BioLegend 100232, 1:100), anti-FoxP3 PE (clone FJK-16s, eBioscience 12-5773-80) 1:100), and anti-Granzyme B APC (clone GB12, Invitrogen, MHGB05, 1:100). Using FoxP3 staining kit prepared as per manufacturer instructions (eBioscience 00-5523-00), two solutions were prepared; i) Fox-Fix (fixation/permeabilization concentrate (cat. 00–5123), diluted 1:4 in fixation/permeabilization diluent—100 µL per sample) and ii) Fox-Wash (permeabilization Buffer (10×) (cat. 00–8333) made to a 1× Stock in H$_2$O). 200 µL of buffy coat cells were plated onto a 96-well round bottom culture plate and centrifuged at 2000 rpm for 2 min at 4 °C. Supernatant was expelled by quickly flicking the media from the plate into the sink and the cell pellet was re-suspended in 50 µL of extracellular mastermix. The plate was then covered and incubated on ice for 30 min before being topped up to 180 µL with FACS buffer and centrifuged at 2000 rpm for 2 min at 4 °C. Supernatant was then expelled and the cell pellet re-suspended in 180 µL FACS buffer and centrifuged at 800 xg for 2 min at 4 °C. This process was then repeated once more and the cell pellet re-suspended in 100 µL Fox-Fix (cat. 00–5123) and incubated on ice, covered, for 30 min. The plate was then washed two more times and the cell pellet re-suspended in 50 µL of intracellular master mix. The plate was then covered and incubated on ice for 30 min before being topped up to 180 µL with Fox-Wash (cat. 00–8333) and centrifuged at 800 xg for 2 min at 4 °C. The plate was then washed twice with Fox Wash and the cell pellet re-suspended in FACS buffer (1% PFA). Samples were stored in the fridge if not analyzed immediately for up to two days.

Supporting Information

Supporting Information is available from the Wiley Online Library or from the author.

Conflict of Interest

The authors declare no conflict of interest.

Data Availability Statement

The data that support the findings of this study are available in the supplementary material of this article or are available from the corresponding author upon reasonable request.

[1] X. Liu, Y. Zhang, Y. Wang, W. Zhu, G. Li, X. Ma, Y. Zhang, S. Chen, S. Tiwari, K. Shi, S. Zhang, H. M. Fan, Y. X. Zhao, X.-J. Liang, *Theranostics* **2020**, *10*, 3793.

[2] P. Wust, B. Hildebrandt, G. Sreenivasa, B. Rau, J. Gellermann, H. Riess, R. Felix, P. M. Schlag, *Lancet Oncol.* **2002**, *3*, 487.

[3] M. Hurwitz, P. Stauffer, *Semin. Oncol.* **2014**, *41*, 714.

[4] R. D. Issels, *Eur. J. Cancer* **2008**, *44*, 2546.

[5] V. Bücklein, C. Limmroth, E. Kampmann, G. Schuebbe, R. Issels, F. Roeder, M. Angele, H. Roland Dürr, T. Knösel, S. Abdel-Rahman, D. Di Gioia, L. H. Lindner, *Sarcoma* **2020**, *2020*, 6901678.

[6] R. D. Issels, L. H. Lindner, J. Verweij, R. Wessalowski, P. Reichardt, P. Wust, P. Ghadjar, P. Hohenberger, M. Angele, C. Salat, Z. Vujaskovic, S. Daugaard, O. Mella, U. Mansmann, H. R. Dürr, T. Knösel, S. Abdel-Rahman, M. Schmidt, W. Hiddemann, K.-W. Jauch, C. Belka, A. Gronchi, *JAMA Oncol.* **2018**, *4*, 483.

[7] V. Vilas-Boas, F. Carvalho, B. Espiña, *Molecules* **2020**, *25*, 2874.

[8] S. K. Sharma, N. Shrivastava, F. Rossi, L. D. Tung, N. T. K. Thanh, *Nano Today* **2019**, *29*, 100795.

[9] D. Haemmerich, P. F. Laeseke, *Int. J. Hyperthermia* **2005**, *21*, 755.

[10] K. F. Chu, D. E. Dupuy, *Nat. Rev. Cancer* **2014**, *14*, 199.

[11] P.-y Pu, Y.-z. Zhang, D.-h. Jiang, *Chin. J. Cancer Res.* **2000**, *12*, 257.

[12] S. S. Evans, E. A. Repasky, D. T. Fisher, *Nat. Rev. Immunol.* **2015**, *15*, 335.

[13] E. A. Repasky, S. S. Evans, M. W. Dewhirst, *Cancer Immunol. Res.* **2013**, *1*, 210.

[14] D. T. Fisher, Q. Chen, J. J. Skitzki, J. B. Muhitch, L. Zhou, M. M. Appenheimer, T. D. Vardam, E. L. Weis, J. Passanese, W.-C. Wang, S. O. Gollnick, M. W. Dewhirst, S. Rose-John, E. A. Repasky, H. Baumann, S. S. Evans, *J. Clin. Invest.* **2011**, *121*, 3846.

[15] R. D. Issels, L. H. Lindner, M. Von Bergwelt-Baildon, P. Lang, C. Rischpler, H. Diem, B. Mosetter, J. Eckl, D. J. Schendel, C. Salat, O. Stötzer, S. Burdach, I. Von Luettichau-Teichert, R. Handgretinger, J. Neumann, T. Kirchner, K. Steiger, M. Boxberg, U. Mansmann, G. Multhoff, E. Noessner, *Int. J. Hyperthermia* **2020**, *37*, 55.

[16] T. Carter, P. Mulholland, K. Chester, *Immunotherapy* **2016**, *8*, 941.

[17] I. Elsayed, X. Huang, M. Elsayed, *Cancer Lett.* **2006**, *239*, 129.

[18] X. Huang, I. H. El-Sayed, W. Qian, M. A. El-Sayed, *J. Am. Chem. Soc.* **2006**, *128*, 2115.

[19] C. Fabbro, H. Ali-Boucetta, T. D. Ros, K. Kostarelos, A. Bianco, M. Prato, *Chem. Commun.* **2012**, *48*, 3911.

[20] M. Shevtsov, G. Multhoff, *Curr. Drug Metab.* **2016**, *17*, 737.

[21] M. Shevtsov, S. Stangl, B. Nikolaev, L. Yakovleva, Y. Marchenko, R. Tagaeva, W. Sievert, E. Pitkin, A. Mazur, P. Tolstoy, O. Galibin, V. Ryzhov, K. Steiger, O. Smirnov, W. Khachatryan, K. Chester, G. Multhoff, *Small* **2019**, *15*, 1900205.

[22] A. K. Gupta, M. Gupta, *Biomaterials* **2005**, *26*, 3995.

[23] R. Weissleder, M. Nahrendorf, M. J. Pittet, *Nat. Mater.* **2014**, *13*, 125.

[24] T. Y. Tang, S. P. S. Howarth, S. R. Miller, M. J. Graves, A. J. Patterson, J.-M. U-King-Im, Z. Y. Li, S. R. Walsh, A. P. Brown, P. J. Kirkpatrick, E. A. Warburton, P. D. Hayes, K. Varty, J. R. Boyle, M. E. Gaunt, A. Zalewski, J. H. Gillard, *J. Am. Coll. Cardiol.* **2009**, *53*, 2039.

[25] M. E. Kooi, V. C. Cappendijk, K. B. J. M. Cleutjens, A. G. H. Kessels, P. J. E. H. M. Kitslaar, M. Borgers, P. M. Frederik, M. J. A. P. Daemen, J. M. A. van Engelshoven, *Circulation* **2003**, *107*, 2453.

[26] J. M. Richards, S. I. Semple, T. J. MacGillivray, C. Gray, J. P. Langrish, M. Williams, M. Dweck, W. Wallace, G. McKillop, R. T. A. Chalmers, O. J. Garden, D. E. Newby, *Circ.: Cardiovasc. Imaging* **2011**, *4*, 274.

[27] J. L. Gaglia, M. Harisinghani, I. Aganj, G. R. Wojtkiewicz, S. Hedgire, C. Benoist, D. Mathis, R. Weissleder, *Proc. Natl. Acad. Sci. U. S. A.* **2015**, *112*, 2139.

[28] V. Weissig, T. Pettinger, N. Murdock, *Int. J. Nanomed.* **2014**, *9*, 4357.

[29] D. Ortega, Q. A. Pankhurst, in *Nanoscience*, Vol. *1*, (Ed: P. O'Brien), RSC Publishing, London **2012**, pp. 60–68.

[30] M. R. A. Abdollah, T. J. Carter, C. Jones, T. L. Kalber, V. Rajkumar, B. Tolner, C. Gruettner, M. Zaw-Thin, J. Baguña Torres, M. Ellis, M. Robson, R. B. Pedley, P. Mulholland, R. T. M. De Rosales, K. A. Chester, *ACS Nano* **2018**, *12*, 1156.

[31] R. Goldstein, J. Sosabowski, M. Livanos, J. Leyton, K. Vigor, G. Bhavsar, G. Nagy-Davidescu, M. Rashid, E. Miranda, J. Yeung, B. Tolner, A. Plückthun, S. Mather, T. Meyer, K. Chester, *Eur. J. Nucl. Med. Mol. Imaging* **2014**, *41*, 1.

[32] J. Echevarria-Uraga, García-Alonso, Plazaola, Insausti, Etxebarria, Saiz-Lopez, Fernández-Ruanova, *Int. J. Nanomed.* **2012**, *7*, 2399.

[33] S. Wilhelm, A. J. Tavares, Q. Dai, S. Ohta, J. Audet, H. F. Dvorak, W. C. W. Chan, *Nat. Rev. Mater.* **2016**, *1*, 16014.

[34] M. Torrice, *ACS Cent. Sci.* **2016**, *2*, 434.

[35] A. Jordan, R. Scholz, K. Maier-Hauff, F. K. H. van Landeghem, N. Waldoefner, U. Teichgraeber, J. Pinkernelle, H. Bruhn, F. Neumann, B. Thiesen, A. Von Deimling, R. Felix, *J. Neuro-Oncol.* **2006**, *78*, 7.

[36] K. Maier-Hauff, F. Ulrich, D. Nestler, H. Niehoff, P. Wust, B. Thiesen, H. Orawa, V. Budach, A. Jordan, *J. Neuro-Oncol.* **2011**, *103*, 317.

[37] K. Maier-Hauff, R. Rothe, R. Scholz, U. Gneveckow, P. Wust, B. Thiesen, A. Feussner, A. Von Deimling, N. Waldoefner, R. Felix, A. Jordan, *J. Neuro-Oncol.* **2007**, *81*, 53.

[38] F. K. H. van Landeghem, K. Maier-Hauff, A. Jordan, K.-T. Hoffmann, U. Gneveckow, R. Scholz, B. Thiesen, W. Brück, A. Von Deimling, *Biomaterials* **2009**, *30*, 52.

[39] T. Kobayashi, K. Kakimi, E. Nakayama, K. Jimbow, *Nanomedicine* **2014**, *9*, 1715.

[40] A. Mukhopadhaya, J. Mendecki, X. Dong, L. Liu, S. Kalnicki, M. Garg, A. Alfieri, C. Guha, *Cancer Res.* **2007**, *67*, 7798.

[41] C. Garrido, M. Brunet, C. Didelot, Y. Zermati, E. Schmitt, G. Kroemer, *Cell Cycle* **2006**, *5*, 2592.

[42] J. R. Ostberg, E. Kabingu, E. A. Repasky, *Int. J. Hyperthermia* **2003**, *19*, 520.

[43] M. Nishikawa, S. Takemoto, Y. Takakura, *Int. J. Pharm.* **2008**, *354*, 23.

[44] P. Li, J. L. Gregg, N. Wang, D. Zhou, P. O'donnell, J. S. Blum, V. L. Crotzer, *Immunol. Rev.* **2005**, *207*, 206.

[45] T. Chen, J. Guo, C. Han, M. Yang, X. Cao, *J. Immunol.* **2009**, *182*, 1449.

[46] M. Shevtsov, G. Multhoff, *Front. Immunol.* **2016**, *7*, 171.

[47] M. Muthana, G. Multhoff, A. Graham Pockley, *Int. J. Hyperthermia* **2010**, *26*, 247.

[48] I. Sato, M. Umemura, K. Mitsudo, H. Nakashima, T. Iwai, X. Feng, K. Oda, A. Miyajima, A. Makino, M. Iwai, T. Fujita, U. Yokoyama, S. Okumura, M. Sato, H. Eguchi, I. Tohnai, Y. Ishikawa, *J. Physiol. Sci.* **2014**, *64*, 177.

[49] A. J. Giustini, R. Ivkov, P. J. Hoopes, *Nanotechnology* **2011**, *22*, 345101.

[50] E. Boros, A. M. Bowen, L. Josephson, N. Vasdev, J. P. Holland, *Chem. Sci.* **2015**, *6*, 225.

[51] B. M. Skinner, E. E. P. Johnson, *Chromosoma* **2017**, *126*, 195.

[52] M. A. Shevtsov, B. P. Nikolaev, V. A. Ryzhov, L. Y. Yakovleva, A. V. Dobrodumov, Y. Y. Marchenko, B. A. Margulis, E. Pitkin, I. V. Guzhova, *J. Magn. Magn. Mater.* **2015**, *388*, 123.

[53] V. Ryzhov, I. Larionov, V. Fomichev, *J. Tech. Phys.* **1996**, *41*, 620.

[54] V. Ryzhov, V. A. Ryzhov, I. A. Kiselev, O. P. Smirnov, Y. P. Chernenkov, V. V. Deriglazov, Y. Y. Marchenko, L. Y. Yakovleva, B. P. Nikolaev, Y. V. Bogachev, arXiv preprint arXiv:1712.07534 **2017**.

[55] E. K. Schlachter, H. R. Widmer, A. Bregy, T. Lönnfors-Weitzel, I. Vajtai, N. Corazza, V. J. P. Bernau, T. Weitzel, P. Mordasini, J. Slotboom, G. Herrmann, S. Bogni, H. Hofmann, M. Frenz, M. Reinert, *Int. J. Nanomed.* **2011**, *6*, 1793.

[56] L.i Li, W. Jiang, K. Luo, H. Song, F. Lan, Y. Wu, Z. Gu, *Theranostics* **2013**, *3*, 595.

[57] C. Xu, D. Miranda-Nieves, J. A. Ankrum, M. E. Matthiesen, J. A. Phillips, I. Roes, G. R. Wojtkiewicz, V. Juneja, J. R. Kultima, W. Zhao, P. K. Vemula, C. P. Lin, M. Nahrendorf, J. M. Karp, *Nano Lett.* **2012**, *12*, 4131.

[58] J. W. M. Bulte, D. L. Kraitchman, *NMR Biomed.* **2004**, *17*, 484.

[59] S. Balivada, R. S. Rachakatla, H. Wang, T. N. Samarakoon, R. K. Dani, M. Pyle, F. O. Kroh, B. Walker, X. Leaym, O. B. Koper, M. Tamura, V. Chikan, S. H. Bossmann, D. L. Troyer, *BMC Cancer* **2010**, *10*, 119.

[60] M. Johannsen, B. Thiesen, A. Jordan, K. Taymoorian, U. Gneveckow, N. Waldöfner, R. Scholz, M. Koch, M. Lein, K. Jung, S. A. Loening, *Prostate* **2005**, *64*, 283.

ADVANCED
SCIENCE NEWS

www.advancedsciencenews.com

NANO · MICRO
small

www.small-journal.com

[61] A. Jordan, R. Scholz, P. Wust, H. Fähling, J. Krause, W. Wlodarczyk, B. Sander, T.h. Vogl, R. Felix, *Int. J. Hyperthermia* **1997**, *13*, 587.

[62] S. J. DeNardo, G. L. DeNardo, A. Natarajan, L. A. Miers, A. R. Foreman, C. Gruettner, G. N. Adamson, R. Ivkov, *J. Nucl. Med.* **2007**, *48*, 437.

[63] G. D. Lianos, G. A. Alexiou, A. Mangano, A. Mangano, S. Rausei, L. Boni, G. Dionigi, D. H. Roukos, *Cancer Lett.* **2015**, *360*, 114.

[64] M. Nishikawa, S. Takemoto, Y. Takakura, *Int. J. Pharm.* **2008**, *354*, 23.

[65] Y. Delneste, V. Larochette, P. Jeannin, in *HSP70 in Human Diseases and Disorders*, Springer, Berlin **2018**, pp. 173–203.

[66] H. M. Beere, B. B. Wolf, K. Cain, D. D. Mosser, A. Mahboubi, T. Kuwana, P. Tailor, R. I. Morimoto, G. M. Cohen, D. R. Green, *Nat. Cell Biol.* **2000**, *2*, 469.

[67] N. R. Datta, S. Krishnan, D. E. Speiser, E. Neufeld, N. Kuster, S. Bodis, H. Hofmann, *Cancer Treat. Rev.* **2016**, *50*, 217.

[68] M. W. Dewhirst, C.-T. Lee, K. A. Ashcraft, *Int. J. Hyperthermia* **2016**, *32*, 4.

[69] T. Weiss, M. Weller, P. Roth, *Expert Rev. Anticancer Ther.* **2016**, *16*, 1087.

[70] N. D. Pennock, J. T. White, E. W. Cross, E. E. Cheney, B. A. Tamburini, R. M. Kedl, *Adv. Physiol. Educ.* **2013**, *37*, 273.

[71] J. Yang, M. Hou, W. Sun, Q. Wu, J. Xu, L. Xiong, Y. Chai, Y. Liu, M. Yu, H. Wang, Z. P. Xu, X. Liang, C. Zhang, *Adv. Sci.* **2020**, *7*, 2001088.

[72] R. C. Mould, A. W. K. Auyeung, J. P. Van Vloten, L. Susta, A. J. Mutsaers, J. J. Petrik, G. A. Wood, S. K. Wootton, K. Karimi, B. W. Bridle, *Sci. Rep.* **2017**, *7*, 8322.

[73] T. F. Gajewski, H. Schreiber, Y.-X. Fu, *Nat. Immunol.* **2013**, *14*, 1014.

[74] S. Spranger, R. M. Spaapen, Y. Zha, J. Williams, Y. Meng, T. T. Ha, T. F. Gajewski, *Sci. Transl. Med.* **2013**, *5*, 200ra116.

[75] K. Catakovic, E. Klieser, D. Neureiter, R. Geisberger, *Cell Commun. Signaling* **2017**, *15*, 1.

[76] M. Ahmadzadeh, L. A. Johnson, B. Heemskerk, J. R. Wunderlich, M. E. Dudley, D. E. White, S. A. Rosenberg, *Blood* **2009**, *114*, 1537.

[77] N. S. Joshi, E. H. Akama-Garren, Y. Lu, D.-Y. Lee, G. P. Chang, A. Li, M. Dupage, T. Tammela, N. R. Kerper, A. F. Farago, R. Robbins, D. M. Crowley, R. T. Bronson, T. Jacks, *Immunity* **2015**, *43*, 579.

[78] L. Zou, H. Wang, B. He, L. Zeng, T. Tan, H. Cao, X. He, Z. Zhang, S. Guo, Y. Li, *Theranostics* **2016**, *6*, 762.

[79] K. P. Tamarov, L. A. Osminkina, S. V. Zinovyev, K. A. Maximova, J. V. Kargina, M. B. Gongalsky, Y. Ryabchikov, A. Al-Kattan, A. P. Sviridov, M. Sentis, A. V. Ivanov, V. N. Nikiforov, A. V. Kabashin, V. Y. Timoshenko, *Sci. Rep.* **2014**, *4*, 7034.

[80] K. Mahmoudi, A. Bouras, D. Bozec, R. Ivkov, C. Hadjipanayis, *Int. J. Hyperthermia* **2018**, *34*, 1316.

[81] P. Walter, D. Ron, *Science* **2011**, *334*, 1081.

[82] B. Frey, E.-M. Weiss, Y. Rubner, R. Wunderlich, O. J. Ott, R. Sauer, R. Fietkau, U. S. Gaipl, *Int. J. Hyperthermia* **2012**, *28*, 528.

[83] S. Toraya-Brown, M. R. Sheen, P. Zhang, L. Chen, J. R. Baird, E. Demidenko, M. J. Turk, P. J. Hoopes, J. R. Conejo-Garcia, S. Fiering, *Nanomed.: Nanotechnol., Biol. Med.* **2014**, *10*, 1273.

[84] A. J. Moy, J. W. Tunnell, *Adv. Drug Delivery Rev.* **2017**, *114*, 175.

[85] C. Wang, L. Xu, C. Liang, J. Xiang, R. Peng, Z. Liu, *Adv. Mater.* **2014**, *26*, 8154.

[86] J. Cano-Mejia, R. A. Burga, E. E. Sweeney, J. P. Fisher, C. M. Bollard, A. D. Sandler, C. R. Y. Cruz, R. Fernandes, *Nanomed.: Nanotechnol., Biol. Med.* **2017**, *13*, 771.

[87] Q. Chen, L. Xu, C. Liang, C. Wang, R. Peng, Z. Liu, *Nat. Commun.* **2016**, *7*, 13193.

[88] Q. Chen, Q. Hu, E. Dukhovlinova, G. Chen, S. Ahn, C. Wang, E. A. Ogunnaike, F. S. Ligler, G. Dotti, Z. Gu, *Adv. Mater.* **2019**, *31*, 1900192.

[89] A. Mantovani, F. Marchesi, A. Malesci, L. Laghi, P. Allavena, *Nat. Rev. Clin. Oncol.* **2017**, *14*, 399.

[90] P.-L. Loyher, J. Rochefort, C. Baudesson De Chanville, P. Hamon, G. Lescaille, C. Bertolus, M. Guillot-Delost, M. F. Krummel, F. M. Lemoine, C. Combadière, A. Boissonnas, *Cancer Res.* **2016**, *76*, 6483.

[91] S. Dimeloe, C. Frick, M. Fischer, P. M. Gubser, L. Razik, G. R. Bantug, M. Ravon, A. Langenkamp, C. Hess, *Eur. J. Immunol.* **2014**, *44*, 3614.

[92] D. J. Huss, A. F. Pellerin, B. P. Collette, A. K. Kannan, L. Peng, A. Datta, B. T. Wipke, J. D. Fontenot, *Immunology* **2016**, *148*, 276.

[93] A. El Andaloussi, Y. Han, M. S. Lesniak, *J. Neurosurg.* **2006**, *105*, 430.